ROYAL SOCIETY
OF CHEMISTRY

PAPER

Dual-ligand europium-based metal–organic frameworks and hydrogels for sensitive ratiometric fluorescent detection of tetracyclines in food

Ruipeng Guo,[*a] Sujiao He,[a] Bing Zhu,[b] Zhiwen Xi,[a] Jiaxin Wang[a] and Mingsha Jie [*b]

Tetracycline (TC) residues in animal-derived foods pose potential risks to human health; thus, the establishment of detection methods with high accuracy, strong sensitivity, and easy operation is of considerable importance. Within the present work, a dual-emission fluorescent probe derived from a dual-ligand europium-based MOF (NH$_2$-BDC-Eu-DPA) was developed and thereafter integrated into a fluorescent hydrogel to enable the rapid detection of TCs in animal-derived foods. The probe uses Eu^{3+} as the metal node, with 2-aminoterephthalic acid (BDC-NH$_2$) and pyridine-2,6-dicarboxylic acid (DPA) as dual ligands. Upon excitation at 260 nm, it exhibits dual fluorescence peaks at 427 nm and 617 nm. TCs can specifically quench the fluorescence at these two wavelengths through the IFE, and the quenching effect at 427 nm is more significant. Quantitative analysis is achieved based on the fluorescence intensity ratio (F_{427}/F_{617}). After optimizing the experimental conditions, this method exhibits a linear detection range of 1–200 µmol L^{-1} for doxycycline hydrochloride (DOX), tetracycline (TC), and oxytetracycline (OTC), with a limit of detection of 31.0 nmol L^{-1}, 29.7 nmol L^{-1}, 35.1 nmol L^{-1}, respectively. In actual sample detection, the spiked recoveries for milk and pork are 91.0–106.8% and 89.7–106.4%, respectively, with a relative standard deviation (RSD) ≤ 6.5%. Furthermore, as the concentration of TCs increases, the intensity of the purple fluorescence emitted by the hydrogel shows a gradual downward trend, showing a good linear relationship. The method possesses high selectivity, anti-interference capability, and rapid response characteristics, providing reliable technical support for on-site monitoring of TC residues in animal-derived foods.

1. Introduction

Tetracyclines (TCs) are among the most widely used and largest-volume classes of antibiotics,[1] primarily including doxycycline hydrochloride (DOX), tetracycline (TC), oxytetracycline (OTC), etc. Due to their advantages, such as broad antimicrobial spectrum, high quality at a low price, and strong antibacterial activity,[2,3] TCs have long been used for the prevention and treatment of microbial infections.[4] TCs are recalcitrant to natural degradation.[5] Excessive or improper use leads to their accumulation in animal-derived foods, and ingestion of these residues can pose health risks, such as liver damage, bacterial resistance, and allergic reactions.[6,7] For the purpose of effectively safeguarding food safety, numerous nations have established explicit rules regarding the maximum residue limits (MRLs) of TCs in food products. As an illustration, the European Union has defined MRLs for TCs at 200 µg kg^{-1} in eggs and 100 µg kg^{-1} in milk.[8] Given this, it is necessary to explore and

develop accurate, highly sensitive, and practically operable detection strategies to achieve effective monitoring of TCs.

Currently, there are numerous methods for detecting TC residues, such as high-performance liquid chromatography (HPLC),[9] ultra-performance liquid chromatography-tandem mass spectrometry (UPLC-MS/MS),[10] surface-enhanced Raman spectroscopy (SERS),[11] and enzyme-linked immunosorbent assay (ELISA).[12] Although these methods possess high sensitivity and specificity, they have drawbacks, including time-consuming procedures, the requirement of sophisticated instruments, and complex sample pretreatment.[13] Consequently, there is a need to establish rapid detection approaches for TCs. Fluorescent sensing strategies, characterized by high sensitivity, rapid response, good selectivity, and straightforward operation, are among the most promising analytical techniques for achieving rapid, low-cost, and on-site detection of antibiotics.[14,15] Metal–organic frameworks (MOFs), endowed with superior chemical stability, high specific surface area, and excellent adsorption performance, offer ideal material support for the efficient implementation of such sensing strategies.[16,17] Lanthanide-based metal–organic frameworks (Ln-MOFs) exhibit advantages such as a substantial Stokes shift, elevated quantum yield, intense visible-light emission, prolonged luminescence lifetime, and luminescence energy.[18–21] Rare earth

[a]School of Intelligent Manufacturing and Equipment, Henan Technical Institute, Zhengzhou 450042, China. E-mail: Guoruipeng007@163.com

[b]College of Food and Bioengineering, Zhengzhou University of Light Industry, Zhengzhou, Henan Province, 450002, P. R. China. E-mail: msjie@zzuli.edu.cn
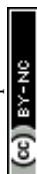
metals (Ln^{3+}), especially europium ions (Eu^{3+}), find extensive application in the fabrication of fluorescent probes, owing to their superior monochromatic properties,[22] pure fluorescence properties,[23] extended luminescent lifetimes,[24] and narrow emission peaks.[25]

However, single emission is susceptible to environmental interference, and intensity changes are difficult to distinguish.[26] Thus, there is an overwhelming need to engineer Ln-MOF probes that exhibit dual emissions upon a single excitation. Dual ligands enable a dual-emission strategy, leveraging the self-calibration of ratiometric detection to mitigate environmental interference, and through distinct color changes, avoid visual fatigue—offering more intuitive visualization than single-fluorescence detection,[27–29] thus exhibiting more intuitive visualization advantages compared with single-fluorescence detection. On the one hand, the synergistic effect of dual ligands provides the MOF with abundant active sites, enabling the efficient enrichment of target antibiotics and laying the foundation for high-sensitivity detection. On the other hand, the dual-emission system reduces environmental interference and improves detection reliability, the emission peaks of the two ligands are significantly different, and the fluorescence color changes obviously with the increase of tetracycline antibiotics concentration, which is convenient for visual detection. This is relatively rare in single-ligand europium-based MOF (Eu-MOF) sensors. The utilization of the MOF as fluorescent sensors for TCs detection complies with the principles of green and sustainable chemistry, featuring minimal reagent consumption and low environmental impact.[30–32] The dual-ligand MOFs provide an accurate and efficient new approach for detecting tetracycline antibiotic residues in intricate matrices, strengthening the defense line of food safety.
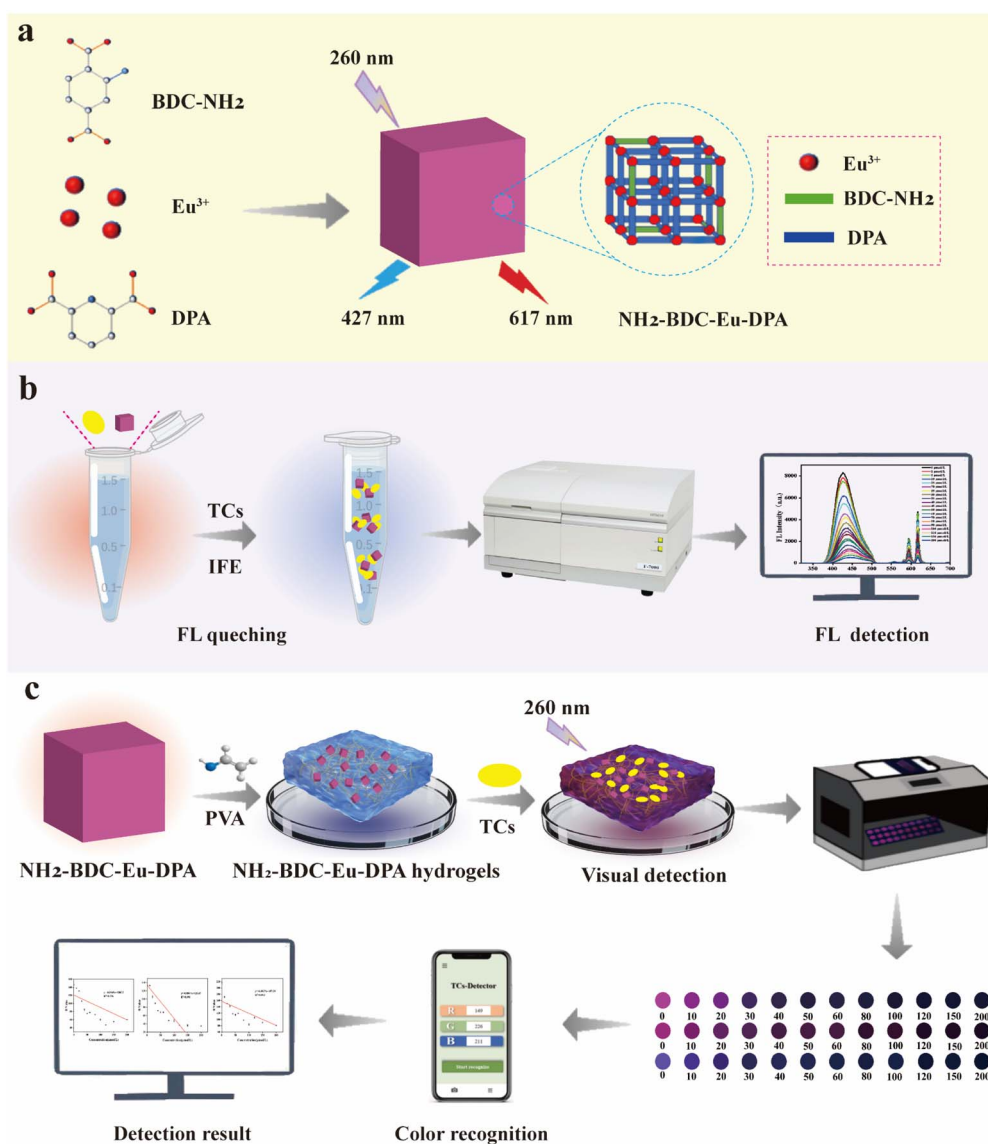
Scheme 1 Schematic illustration of the preparation and formation of NH$_2$-BDC-Eu-DPA (a); schematic diagram depicting the detection of TCs *via* the proposed NH$_2$-BDC-Eu-DPA fluorescent sensor (b); schematic illustration of the visual detection of TCs using NH$_2$-BDC-Eu-DPA fluorescent hydrogels (c).

Based on the above description, as shown in Scheme 1a, an NH$_2$-BDC-Eu-DPA fluorescent probe and its corresponding hydrogel were fabricated with Eu^{3+} serving as the metal node and 2-aminoterephthalic acid (BDC-NH$_2$) acting as the first ligand, which exhibits blue fluorescence and pyridine-2,6-dicarboxylic acid (DPA) as the second ligand (capable of efficiently sensitizing Eu^{3+} ions). This system was applied for the TCs detection. Eu-DPA exhibits only a single red fluorescence specific to Eu^{3+}; whereas, upon the introduction of BDC-NH$_2$, which possesses blue fluorescence, the NH$_2$-BDC-Eu-DPA system achieves dual-emission fluorescent properties. When excited with a single wavelength of 260 nm, the NH$_2$-BDC-Eu-DPA composite demonstrates dual emission signals at 427 nm and 617 nm, which correspond to blue and red fluorescent emissions respectively (Scheme 1b). TCs can quench the fluorescence at 427 nm and 617 nm, with a more significant quenching effect at 427 nm. As the concentration of TCs (DOX, TC, and OTC) rises, the fluorescence emission intensity of NH$_2$-BDC-Eu-DPA decreases in a concentration-dependent manner, and there is a significant linear correlation between them. Furthermore, by fabricating it into a hydrogel, visual detection of TCs is achieved. Through the visual observation of fluorescent color changes and the use of a smartphone-based red-green-blue (RGB) color recognition tool (the color picker application), quantitative visual detection of TCs can be accomplished (Scheme 1c). As a fluorescent probe, NH$_2$-BDC-Eu-DPA additionally exhibits benefits including strong specificity, favorable anti-interference ability, quick response, and a low detection limit when targeting DOX, TC, and OTC.

2. Materials and methods

2.1. Materials and measurements

Europium chloride hexahydrate (EuCl$_3$·6H$_2$O), BDC-NH$_2$, and triethylamine were acquired from Shanghai Aladdin Biochemical Technology Co., Ltd. Meanwhile, DPA was sourced from Shanghai Yuanye Biotechnology Co., Ltd, and anhydrous ethanol was procured from Tianjin Fuyu Fine Chemical Co., Ltd. DOX, TC, OTC, metronidazole (MTZ), lincomycin (LIN), neomycin (NEO), kanamycin sulfate (KANA), florfenicol (FFC), streptomycin sulfate (STR), gentamicin sulfate (GEN), and erythromycin (EM) were obtained from Sangon Biotech Shanghai Co., Ltd. Meanwhile, milk and pork were acquired from local supermarkets, and all remaining reagents were of analytical grade.

A fluorescence spectrophotometer (Hitachi F-7000, Japan) was used to determine fluorescence spectra. Ultraviolet-visible (UV-vis) absorption spectra were documented with a TU-1810 UV-vis spectrophotometerS (Beijing Purkinje General Instrument Co., Ltd, China). An FT-IR spectrophotometer (Antaris II, USA) was employed to obtain Fourier transform infrared (FT-IR) spectra. Morphological images were obtained through a JSM-7001F scanning electron microscope (JEOL, Japan). X-ray diffraction (XRD) patterns were generated using a multifunctional X-ray diffractometer (Ultima IV, Japan). Meanwhile, X-ray photoelectron spectroscopy (XPS) data were gathered with a Thermo Scientific K-Alpha spectrometer (Thermo Fisher Scientific, USA).

2.2. Synthesis of NH$_2$-BDC-Eu-DPA

NH$_2$-BDC-Eu-DPA was synthesized with slight modifications based on previous literature.[33] A one-pot method was adopted for the synthesis of NH$_2$-BDC-Eu-DPA. EuCl$_3$·6H$_2$O (0.25 mmol, 91.5 mg) was dissolved in 5 mL of ultrapure water. DPA (0.5 mmol, 83.6 mg) and BDC-NH$_2$ (0.25 mmol, 54.3 mg) were added to 15 mL of ethanol containing 101.2 mg of triethylamine, and the mixture underwent sonication until it was fully dissolved. Subsequently, the two solutions were combined in a round-bottom flask and agitated at 40 °C for 2 h. After cooling to room temperature, the mixture was centrifuged to remove the solvent. The precipitate was rinsed three times with ethanol to remove excess ligands and unreacted metal ions. Eventually, the product was placed in a drying oven for overnight dehydration.

2.3. Preparation of NH$_2$-BDC-Eu-DPA hydrogel sensor

A hydrogel sensor based on NH$_2$-BDC-Eu-DPA was prepared via the freeze-thaw method.[34] First, 1.5 g of PVA-1799 was dissolved in 10.5 g of deionized water; the mixture was continuously heated to 95 °C and stirred constantly for 3 h to ensure complete dissolution. The obtained solution was ultrasonicated for 15 min to remove air bubbles, thus forming a homogeneous and transparent PVA solution. After that, a 2 mg mL^{-1} NH$_2$-BDC-Eu-DPA solution was added to the PVA solution, and the mixture was magnetically stirred at room temperature for 10 min before being left to stand for further bubble elimination. The NH$_2$-BDC-Eu-DPA-containing mixed solution was poured into a glass Petri dish and subjected to three freeze-thaw cycles–each cycle involved freezing at −20 °C for 20 h and subsequent thawing at 25 °C for 4 h. Finally, the prepared NH$_2$-BDC-Eu-DPA hydrogel sensor was shaped into uniform circular forms using a patterned mold.

2.4. Fluorescent ratiometric detection of TCs

The settings for fluorescence emission spectra and excitation spectra were as follows: For the emission spectrum mode, a fixed excitation wavelength of 260 nm was used; for the excitation spectrum mode, a fixed emission wavelength of 617 nm was adopted. The photomultiplier tube voltage was maintained at 700 V, with a scanning rate of 1200 nm min^{-1}, a slit width of 5 nm, and an integration time of 0.1 s. The full wavelength range covered was 200–800 nm.

DOX, TC, and OTC were each mixed with NH$_2$-BDC-Eu-DPA material at equal ratios at gradient concentrations. Under the optimized experimental conditions, fluorescence spectroscopy was used for detection, with each concentration gradient measured in triplicate in parallel. Based on the detection results, the quantitative relationship between the fluorescence quenching effect induced by the three antibiotics and their concentrations was analyzed, and the standard curves were further established.

To evaluate the specificity of the detection system for DOX, TC, and OTC, 12.5 µg mL^{-1} NH$_2$-BDC-Eu-DPA, 100 µmol L^{-1} TCs (DOX, TC, and OTC), and 100 µmol L^{-1} of 8 interfering

antibiotics (MTZ, LIN, NEO, KANA, FFC, STR, GEN and EM) were mixed at a volume ratio of 2:1:1. The fluorescence intensity of the mixed solution was determined to examine how other antibiotics affect the detection process.

Considering the common complex scenario where multiple ions and biological macromolecules coexist in actual sample matrices, 12.5 μg mL^{-1} NH$_2$-BDC-Eu-DPA was mixed with 100 μmol L^{-1} anions, cations, and biological macro-molecules (Na$^+$, Mg^{2+}, Ca^{2+}, Cl$^-$, NO$_3^-$, SO$_4^{2-}$, lactose, proline, glycine, serine) at a volume ratio of 1:1. Their fluo-rescence intensity was detected to assess the anti-interference capability of the material. Additionally, 0.0125 mg per mL NH$_2$-BDC-Eu-DPA, 100 μmol L^{-1} TCs (DOX, TC, and OTC), and 100 μmol L^{-1} anions, cations, and biological macromolecules were mixed at a volume ratio of 2:1:1. The fluorescence intensity of the mixed solution was measured to examine how anions, cations, and biological macromolecules affect the detection process.

2.5. Determination of TCs resides in milk and pork samples

Milk sample treatment: 5.0 mL of the milk sample was sub-jected to deproteinization. Acetonitrile was added at a volume ratio of 1:1, followed by ultrasonic-assisted extraction for 10 min. Centrifugation of the mixed system was carried out at 10 000 rpm for a duration of 10 min. Following this, the supernatant was gathered and filtered with a 0.22 μm micro-porous filter membrane to get rid of particles. The filtrate ob-tained was diluted 10 times in ultrapure water, thus preparing the stock solution for detection purposes.[35] The source where we purchased the milk and pork samples we used for the experiment in the main article was the local Dazhang supermarket.

Pork sample treatment: accurately weigh 2.00 g of homog-enized sample into a 50 mL centrifuge tube, add 10.0 mL of acetonitrile extract containing 1% formic acid, vortex for 1 min, and then perform ultrasonic extraction for 30 min. Add 1.0 g of sodium chloride and 4.0 g of anhydrous magnesium sulfate to the mixed system, vortex for 5 min, and then centrifuge at 10 000 rpm for 10 min. Transfer the supernatant, then add 50 mg of PSA adsorbent, 150 mg of C18 packing material, and 900 mg of sodium sulfate. After shaking for 5 min for purification, centrifuge again (10 000 rpm, 5 min). Precisely transfer 7.0 mL of the purified solution, blow it to near dryness under a nitrogen atmosphere at 40 °C, quanti-tatively add 7.0 mL of acetonitrile solvent for reconstitution, vortex for 5 min, and assist dissolution with ultrasonics for 10 min, and finally filter through a 0.22 μm microporous filter membrane is used for filtration, thereby acquiring the sample required for analysis.[36]

For the spiking experiment, the NH$_2$-BDC-Eu-DPA fluores-cent material, the treated milk and pork sample matrices, and different concentrations of DOX, TC, and OTC were mixed uniformly at a volume ratio of 2:1:1. Three antibiotic concentrations (low, medium, and high) were selected to calculate the recoveries and relative standard deviations (RSD) of the three antibiotics in pork and milk samples.

3. Results and discussion

3.1. Characterizations of NH$_2$-BDC-Eu-DPA

The europium-based MOFs NH$_2$-BDC-Eu-DPA are fabricated with Eu^{3+} as the metal node and BDC-NH$_2$ and DPA as dual ligands. Scanning electron microscopy (SEM) images (Fig. 1a and b) reveal that NH$_2$-BDC-Eu-DPA exhibits a rod-like morphology. Meanwhile, the energy-dispersive spectroscopy (EDS) analysis (Fig. 1c and S1a) demonstrates that the elements C, N, O, and Eu are evenly dispersed throughout the nano-material. Among them (Fig. S1b and Table S2), C atoms account for the largest mass fraction and atomic fraction of the material, which are 51.40% and 62.73%, respectively.

Further characterization via XRD (Fig. 1d) showed that NH$_2$-BDC-Eu-DPA had diffraction peaks at 7.2°, 9.36°, 15.72°, 16.36°, 19.76°, 31.64°, and 32.96°. The sharp and prominent diffraction peaks near 9.36°, 16.36°, 19.76°, and 32.96° were indexed to the (022), (111), (521), and (666) lattice planes.

The porosity of NH$_2$-BDC-Eu-DPA was examined through the use of N$_2$ adsorption–desorption isotherms. As shown in Fig. 1e, the adsorption isotherm of NH$_2$-BDC-Eu-DPA fits the type I/IV classification, and an H4 hysteresis loop is detected under higher relative pressures, which suggests that both micropores and mesopores exist within the material.[37,38] The data show that the specific surface area of NH$_2$-BDC-Eu-DPA is 58.3590 m^2 g^{-1}. In addition, pore size analysis was performed using density functional theory (DFT) and Barrett–Joyner–Halenda (BJH) methods, and the results (Fig. S2a and S2b) confirm the existence of micropores and mesopores in the NH$_2$-BDC-Eu-DPA nanohybrid.[39,40] As a result, the substantial specific surface area and porous structure of this material are capable of offering ample active sites for high-sensitivity sensing, a feature that contributes to enhancing the sensing performance.

The parameters of the FT-IR spectrometer were set, and the spectra of NH$_2$-BDC-Eu-DPA, ligands BDC-NH$_2$ and DPA were collected in the wavenumber range of 400–4000 cm^{-1} using the attenuated total reflection mode with background correc-tion. It can be seen from Fig. 1f that the broad band at 2500–3000 cm^{-1} disappears in NH$_2$-BDC-Eu-DPA, indicating that DPA and BDC-NH$_2$ undergo complete deprotonation, thereby forming the MOF. In DPA and BDC-NH$_2$, the peaks located at 1704.5 cm^{-1} and 1690.3 cm^{-1} are attributed to the stretching vibrations of the C=O bonds in carboxyl groups, but a red shift is observed in NH$_2$-BDC-Eu-DPA. These changes indicate that the carboxylate groups coordinate with Eu^{3+} ions to form the MOF.

The elemental composition and chemical states of the material were investigated via XPS. The XPS survey spectrum of NH$_2$-BDC-Eu-DPA (Fig. 1g) indicates the presence of Eu, O, N, and C as the main elements. Meanwhile, high-resolution spectra of each element were analyzed. In the Eu 3d spectrum (Fig. 2a), the peaks at 1124.94 eV and 1134.86 eV correspond to Eu 3d$_{5/2}$, while those at 1115.15 eV and 1164.5 eV correspond to Eu 3d$_{3/2}$. In the C 1s spectrum (Fig. 2b), three peaks at 284.9 eV, 285.87 eV, and 288.54 eV are assigned to C–C/C=C, C–O–C, and
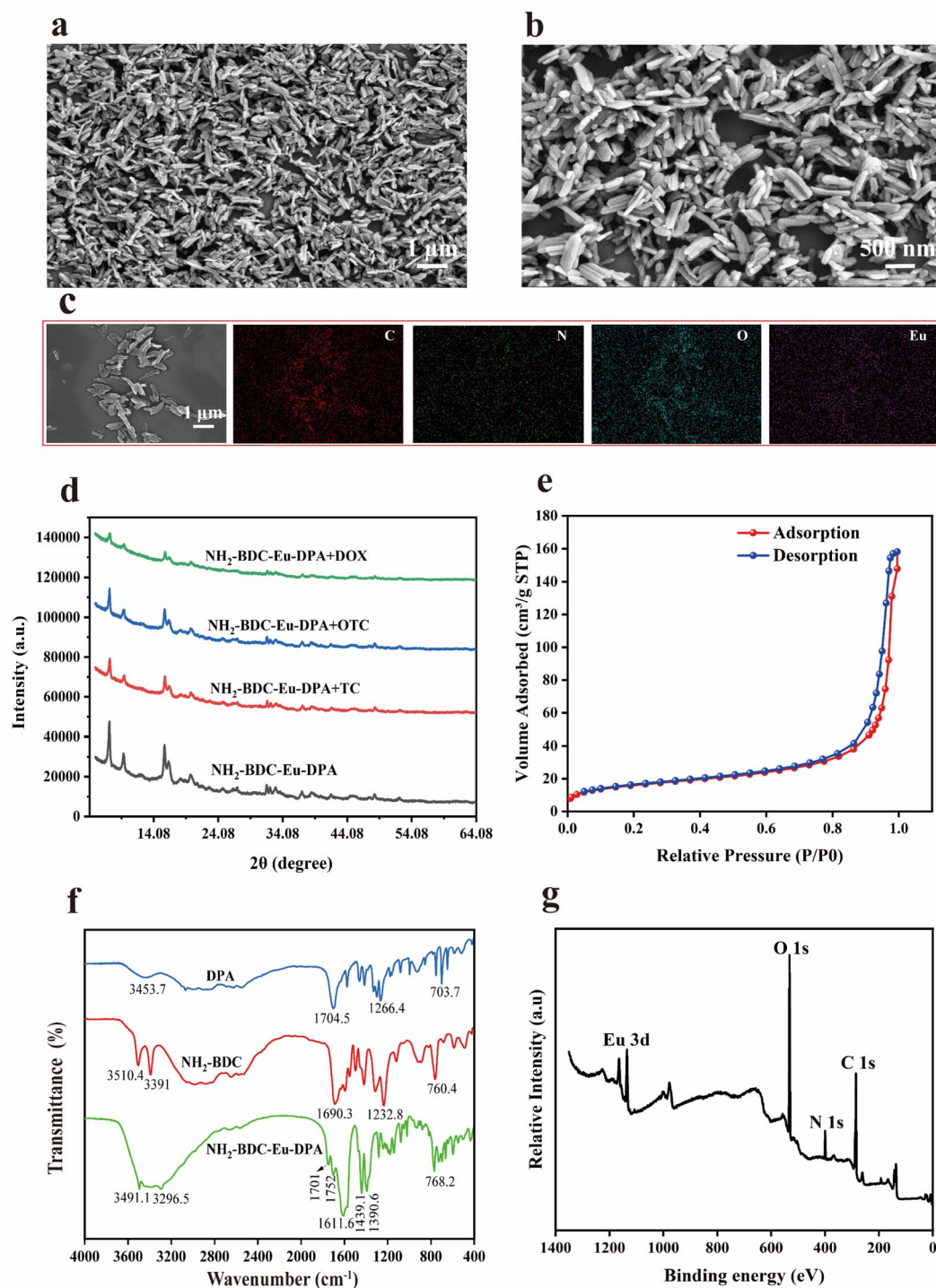
Fig. 1 SEM images (a) and high-resolution (b) SEM of NH_2-BDC-Eu-DPA; EDS mapping image of NH_2-BDC-Eu-DPA (c); XRD pattern of NH_2-BDC-Eu-DPA and after binding with TCs (d); N_2 adsorption–desorption isotherm (e); FT-IR spectra of DAP, NH_2-BDC, NH_2-BDC-Eu-DPA (f); XPS survey spectrum (g).

C=O, respectively. In the O 1s spectrum (Fig. 2c), three peaks at 531.33 eV, 532.25 eV, and 533.20 eV correspond to C=O, C–O, and O–H, respectively. In the N 1s spectrum (Fig. 2d), two peaks at 399.05 eV and 399.68 eV are attributed to N–H and N–C, respectively. These results confirm the successful synthesis of NH_2-BDC-Eu-DPA.

3.2. Optical properties of NH_2-BDC-Eu-DPA

As shown in Fig. 3a, UV-vis spectroscopic analysis indicates that NH_2-BDC-Eu-DPA has characteristic absorption peaks at 271 and 278 nm. Meanwhile, DOX presents absorption peaks at 263 and 338 nm, TC shows three absorption peaks at 271 nm,
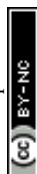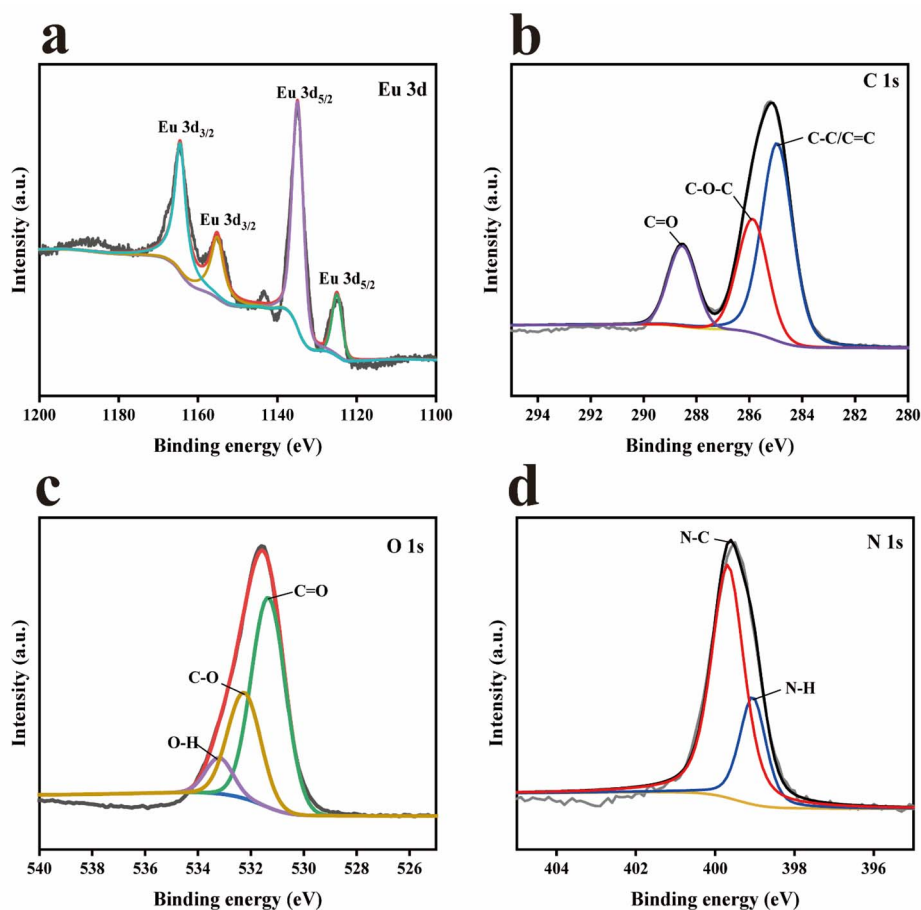
Fig. 2 High-resolution XPS spectra: Eu 3d (a), C 1s (b), O 1s (c), N 1s (d).

278 nm, and 345 nm, and OTC exhibits characteristic absorption peaks at 264 and 302 nm. When NH$_2$-BDC-Eu-DPA forms composite systems with TCs, their absorption peaks are mainly concentrated in the ranges of 270–280 nm and 310–360 nm.

The ultraviolet-visible absorption (Abs) and fluorescence (E_m, E_x) spectra of NH$_2$-BDC-Eu-DPA (Fig. 3b) indicate that the fluorescent material NH$_2$-BDC-Eu-DPA has characteristic absorption peaks at 224 nm, 271 nm, and 278 nm. The fluorescence excitation spectrum exhibits characteristic absorption peaks at 224 nm, 252 nm, and 327 nm. As for the fluorescence emission spectrum, it shows characteristic absorption peaks at 425 nm, 594 nm, and 617 nm, with these peaks being emitted by
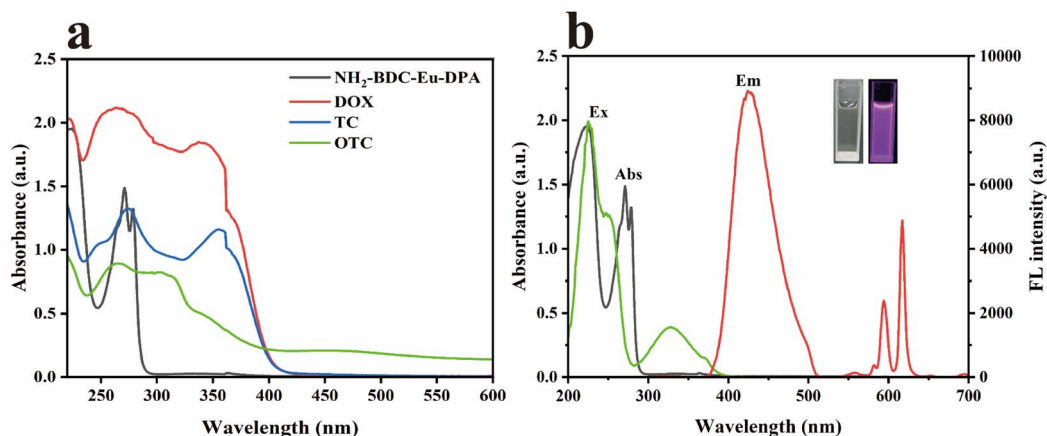

Fig. 3 UV-vis absorption spectra (a) and fluorescence spectra (b) of each detection system.

Eu^{3+}. Furthermore, in the inset of Fig. 2b, the left panel shows the NH$_2$-BDC-Eu-DPA solution without UV irradiation, whereas the right panel presents the NH$_2$-BDC-Eu-DPA solution irradiated at 260 nm, which exhibits a blue-purple color. When excited at a wavelength of 260 nm and within a scanning range of 200–800 nm, NH$_2$-BDC-Eu-DPA shows two emission peaks located at 427 and 617 nm.

3.3. Optimization of the detection conditions

To improve the sensitivity of the probe NH$_2$-BDC-Eu-DPA for detecting DOX, TC, and OTC, further investigations were conducted on the effects of excitation wavelength, ionic strength, pH value, photobleaching resistance, and reaction time on the detection performance. Firstly, the excitation wavelength was studied. As shown in Fig. S3a, with the red shift of the excitation wavelength (250–275 nm), the fluorescence emission intensity at 427 nm decreased, while that at 617 nm increased. When the excitation wavelength was set to 260 nm, NH$_2$-BDC-Eu-DPA exhibited dual-emission characteristics, showing both red and blue fluorescence. As a result, 260 nm was chosen as the most suitable excitation wavelength. Secondly, the ionic strength was examined in the present work. As presented in Fig. S3b, the fluorescence intensity of NH$_2$-BDC-Eu-DPA showed no significant changes in NaCl solutions with logarithmic gradient concentrations (0, 1, 10, 100, 1000 μmol L^{-1}). The experimental data indicated that NH$_2$-BDC-Eu-DPA remained stable and exhibited good salt tolerance within the NaCl concentration range of 0–1000 μmol L^{-1}.

To screen out the optimal pH for NH$_2$-BDC-Eu-DPA, the fluorescent material was mixed with solutions of different pH values in equal volumes, and the changes in fluorescence emission peak intensity were monitored. As shown in Fig. S3c, the intensity of the emission peak at 427 nm attained its maximum value under a pH condition of 8; thus, 8 was determined as the optimal pH. Within the optimized reaction system, 20 min continuous dynamic photobleaching assay was conducted, with the excitation wavelength adjusted to 260 nm and the emission wavelengths set at 427 and 617 nm, respectively. Based on the fluorescence stability test data in Fig. S3d, NH$_2$-BDC-Eu-DPA exhibited stable fluorescence emission under continuous irradiation, confirming its excellent photobleaching resistance and photophysical stability. Finally, the reaction time of the probe was examined. As depicted in Fig. S3e, NH$_2$-BDC-Eu-DPA reached steady-state fluorescence emission at 7 min, and the composite systems of the fluorescent material with the three antibiotics maintained stable emission signals within 0–15 min. The fluorescent material NH$_2$-BDC-Eu-DPA showed a rapid response to TCs, so the detection time parameter was optimized to 7 min.

3.4. Detection mechanism of NH$_2$-BDC-Eu-DPA

NH$_2$-BDC-Eu-DPA exhibits excellent detection performance for TCs, which drives us to deeply explore its sensing mechanism. Multiple action mechanisms, such as the inner filter effect (IFE),[41] fluorescence resonance energy transfer (FRET),[42] and electron transfer[43] may all lead to the occurrence of the

fluorescence quenching phenomenon. The UV-Vis absorption spectra of DOX, TC, and OTC solutions show substantial overlap with the fluorescence excitation spectrum of NH$_2$-BDC-Eu-DPA (Fig. 3b), which suggests that IFE is the primary factor contributing to fluorescence quenching. The UV-Vis absorption spectra of DOX, TC, and OTC solutions hardly overlap with the emission spectrum of NH$_2$-BDC-Eu-DPA, thus excluding the possibility of fluorescence quenching caused by FRET. Compared with the characteristic absorption peaks of NH$_2$-BDC-Eu-DPA and the TCs alone, the characteristic absorption peaks of the NH$_2$-BDC-Eu-DPA-antibiotic composite systems show obvious changes (Fig. 4a). After NH$_2$-BDC-Eu-DPA binds to TCs (DOX, TC, and OTC), the absorption peaks generally exhibit a red-shift trend (with differences in the degree of red-shift among different TCs), confirming the occurrence of binding reactions between them.

The XRD patterns of NH$_2$-BDC-Eu-DPA remain unchanged before and after its binding with DOX, TC, and OTC (Fig. 1d), indicating that the material's basic structure stays unchanged when detecting TCs (DOX, TC, and OTC). Therefore, the alteration in fluorescence intensity does not stem from the disruption of the crystalline structure of NH$_2$-BDC-Eu-DPA. As shown in Fig. S4a, tetracyclines have characteristic peaks at 3405–3452 cm^{-1} and 1607–1626 cm^{-1}. As shown in Fig. 4b, compared with the FT-IR spectrum of NH$_2$-BDC-Eu-DPA, after mixing NH$_2$-BDC-Eu-DPA with tetracyclines, the characteristic peaks at 1701 cm^{-1} and 1752 cm^{-1} disappear, and the positions and intensities of other characteristic peaks change. These changes indicate that a reaction has occurred between NH$_2$-BDC-Eu-DPA and TCs (Fig. S5). Meanwhile, the variations in the fluorescence lifetimes of NH$_2$-BDC-Eu-DPA at 427 and 617 nm were tracked both prior to and following the introduction of DOX, TC, and OTC (Fig. 4c and d), with the fitted lifetimes and corresponding parameters summarized in Table S3. The fluorescence lifetimes of NH$_2$-BDC-Eu-DPA at 427 and 617 nm are 14.9 ns and 456.9 μs, respectively. No significant changes in fluorescence lifetimes were observed upon the introduction of DOX, TC, and OTC, which further confirms that the fluorescence quenching is induced by IFE. The quenching type was further verified using the Stern–Volmer equation. The calculated Stern–Volmer constants (K_{SV}) for DOX, TC, and OTC are 9.3×10^6 L mol^{-1}, 9.3×10^6 L mol^{-1}, and 8.9×10^6 L mol^{-1}, respectively (Fig. S6). Based on these K_{SV} values and the intrinsic lifetime (τ_0), the quenching rate constants (K_q) were determined to be 2.04×10^{10} L (mol^{-1} s^{-1}), 2.04×10^{10} L (mol^{-1} s^{-1}), and 1.88×10^{10} L (mol^{-1} s^{-1}), all of which exceed the maximum value for dynamic quenching (1.0×10^{10} L (mol^{-1} s^{-1})). These results confirm that static quenching dominates the fluorescence quenching process. In conclusion, the fluorescence quenching mechanism is associated with IFE.

3.5. Fluorescent detection of DOX, TC, and OTC using NH$_2$-BDC-Eu-DPA

Under the optimal experimental conditions, with the gradual increase in the concentration gradients of DOX, TC, and OTC, the fluorescence emission intensity of NH$_2$-BDC-Eu-DPA
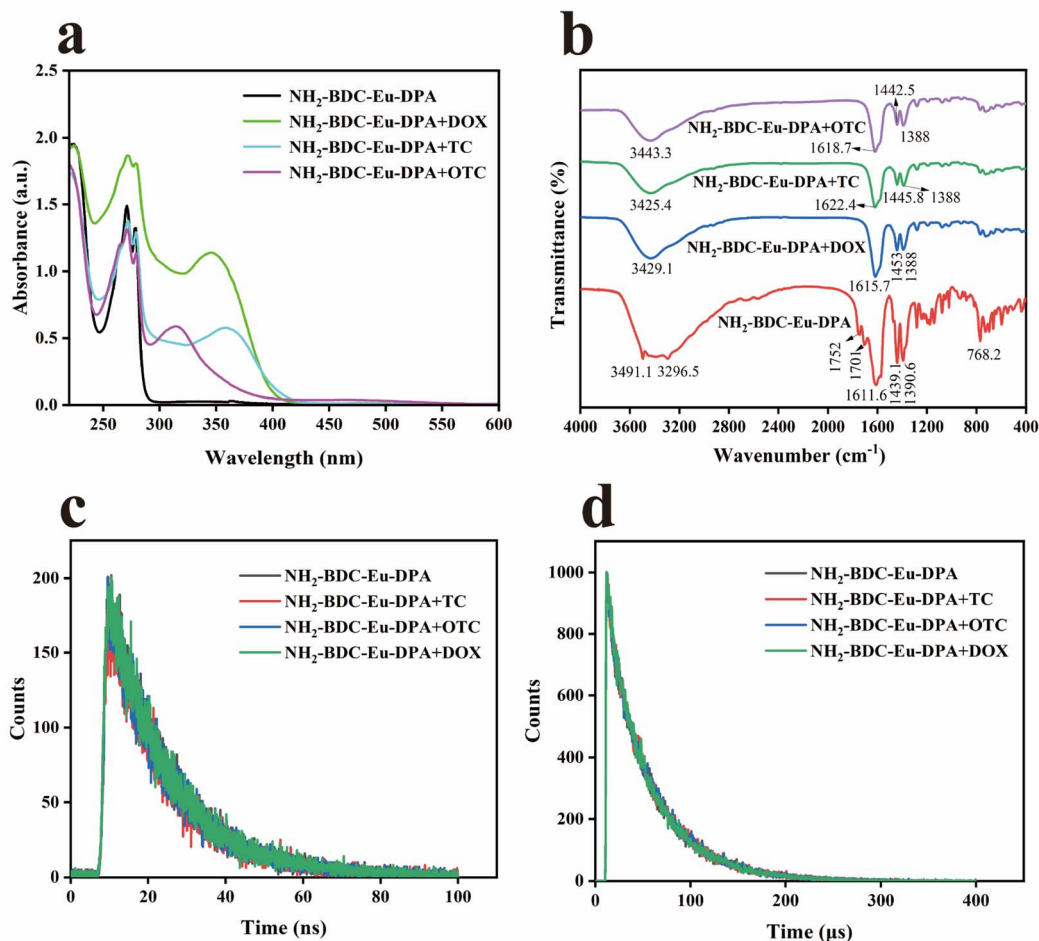
Fig. 4 UV-vis absorption spectra of before and after binding with TCs (a); NH$_2$-BDC-Eu-DPA after binding with TCs (b); fluorescence lifetime changes at wavelengths of 427 nm (c) and 617 nm (d).

showed a concentration-dependent decrease (Fig. 5a–c), and the fluorescence quenching effect at 427 nm was more significant than that at 617 nm. A quantitative detection model was established using the fluorescence signal attenuation values and the concentrations of DOX, TC, and OTC. Within the dynamic range of 1–200 μmol L^{-1}, a robust linear correlation was found to exist between the DOX concentration and the F_{427}/F_{617} ratio (Fig. 5d), with the fitting equation being $y = 0.06069x - 2.92077$ ($R^2 = 0.993$). Similarly, a good linear correlation was observed between the TC concentration and F_{427}/F_{617} (Fig. 5e), with the fitting equation $y = 0.02292x + 1.38625$ ($R^2 = 0.993$). For OTC, a good linear correlation was also found between its concentration and F_{427}/F_{617} (Fig. 5f), with the fitting equation $y = 0.02998x + 3.05266$ ($R^2 = 0.996$). The detection limits of DOX, TC, and OTC are 31.0 nmol L^{-1}, 29.7 nmol L^{-1}, 35.1 nmol L^{-1}, respectively. As the concentrations of DOX, TC, and OTC continuously increase, the purple fluorescence of the NH$_2$-BDC-Eu-DPA solution continuously weakens, as shown in the inset figures in Fig. 5d–f. In addition, Fig. 5g–i show the chromaticity diagrams of NH$_2$-BDC-Eu-DPA in the presence of DOX, TC, and OTC, confirming that under 260 nm UV irradiation, as the concentration of TCs continuously increases, the fluorescence intensity gradually decreases. Table S4 summarizes some

previous detection methods for tetracycline antibiotics. Compared with these previous methods, the proposed method exhibits advantages such as a wide linear detection range, high sensitivity, and rapid operation for the detection of DOX, TC, and OTC. Therefore, the NH$_2$-BDC-Eu-DPA fluorescent probe can be effectively used for the detection of TCs.

To evaluate the selectivity of the detection system for DOX, TC, and OTC, 8 interferents (MTZ, LIN, NEO, KANA, FFC, STR, GEN, and EM) were selected for selectivity verification. Three groups of systems were set up in the experiment: pure water (blank sample), 100 μmol L^{-1} of the above antibiotics, and DOX, TC, and OTC, each mixed with NH$_2$-BDC-Eu-DPA in equal volumes. The response signal intensity of the composite systems was quantitatively determined using a fluorescence spectrophotometer, with the corresponding fluorescence intensity ratio $\Delta F_{427}/F_{617}$ ((F_0-F_{427})/F_{617}, where F_0 refers to F_{427} of the blank control). As shown in Fig. 6a, DOX, TC, and OTC caused significant fluorescence quenching of NH$_2$-BDC-Eu-DPA; the quenching effect of other antibiotics was significantly weaker than that of DOX, TC, and OTC. These results indicate that NH$_2$-BDC-Eu-DPA has high specificity for DOX, TC, and OTC.
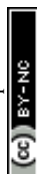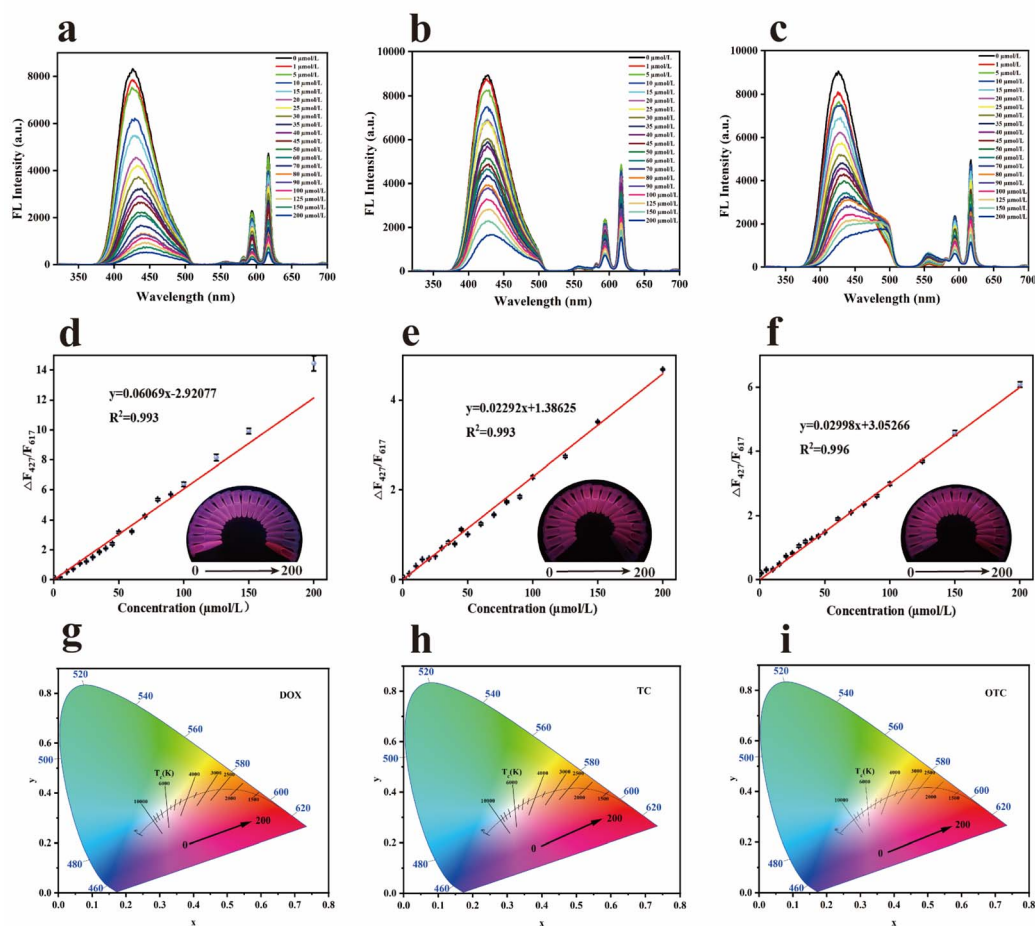
Fig. 5 Fluorescence spectra of DOX (a), TC (b), and OTC (c) at different concentrations; linear relationships between fluorescence intensity and concentrations of DOX (d), TC (e), and OTC (f); the color parameters of NH_2-BDC-Eu-DPA upon the addition of different concentrations of DOX (g), TC (h), and OTC (i) are presented on the CIE chromaticity coordinates diagram, respectively.
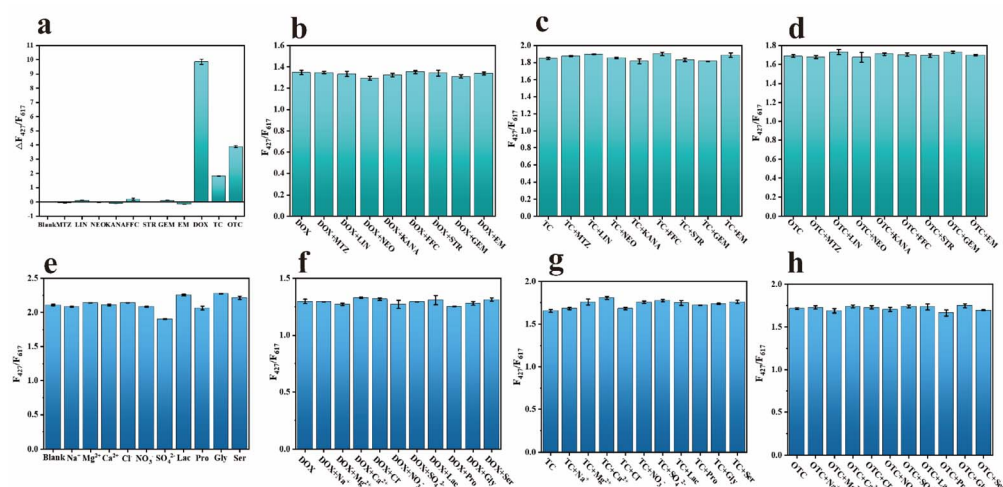

Fig. 6 Selectivity detection of NH_2-BDC-Eu-DPA (a); detection of DOX (b), TC (c), and OTC (d) in the presence of other antibiotics. Anti-interference analysis of NH_2-BDC-Eu-DPA (e); detection of DOX (f), TC (g), and OTC (h) in the presence of interfering substances.

The anti-interference ability of NH_2-BDC-Eu-DPA was investigated in the presence of other antibiotics, anions, cations, and biological macromolecules. As shown in Fig. 6b–d, when NH_2-BDC-Eu-DPA was used to detect DOX, TC, and OTC in the presence of other antibiotics, its F_{427}/F_{617} showed almost no change compared with the blank control. Similarly, the F_{427}/F_{617} of NH_2-BDC-Eu-DPA fluorescent material remained almost unchanged in the presence of anions, cations, and biological macromolecules. As shown in Fig. 6e–h, when NH_2-BDC-Eu-DPA was used to detect DOX, TC, and OTC in the presence of interfering substances, its F_{427}/F_{617} exhibited almost no change compared with the blank control.

In summary, the fluorescence emission intensity of NH_2-BDC-Eu-DPA remains stable in the presence of other antibiotics, anions, cations, and biological macromolecules. Moreover, the coexistence of these interfering substances with DOX, TC, and OTC does not affect the fluorescence quenching effect of NH_2-BDC-Eu-DPA, indicating that NH_2-BDC-Eu-DPA has good anti-interference ability.

3.6. Visual detection of TCs by fluorescent hydrogels

An investigation was conducted into the visual sensing performance of NH_2-BDC-Eu-DPA hydrogel with respect to TCs. The hydrogels exhibited intense and unique purple color under 260 nm UV irradiation. It was visually observed that the fluorescence of the hydrogel underwent quenching to varying degrees; specifically, after the hydrogel-based sensor was respectively immersed in DOX, TC, and OTC solutions with concentrations ranging from 0 to 200 μmol L^{-1}, its purple luminescence gradually weakened (Fig. 7a). An application installed on a smart phone was used to digitize the fluorescence color images, and this application detected the concentrations of DOX, TC and OTC using RGB values. It can be seen from

Fig. 7b–d that the extracted R/B values showed a good linear relationship with the concentrations (0–200 μmol L^{-1}) of DOX ($R^2 = 0.979$), TC ($R^2 = 0.993$), and OTC ($R^2 = 0.995$). The visual detection LOD values of DOX, TC, and OTC are 45.0 nmol L^{-1}, 39.0 nmol L^{-1}, and 17.0 nmol L^{-1}, respectively. In short, the fluorescence sensor based on hydrogel boasts the merits of convenience, rapidity, and high efficiency. As a result, it stands out as a promising means for the visual determination of TCs levels.

3.7. Detection of DOX, TC, and OTC in actual samples

Spiking experiments were conducted by uniformly mixing NH_2-BDC-Eu-DPA fluorescent material, treated milk and pork sample matrices, and different concentrations of DOX, TC, and OTC at a volume ratio of 2 : 1 : 1. Three antibiotic concentrations (low, medium, and high) were selected for the spiking tests. The recoveries and relative standard deviations (RSD) of the three antibiotics in milk and pork samples were calculated. The results of these experiments are shown in Table 1.

The proposed method was applied to detect the low, medium, and high concentrations of the samples. The recoveries of DOX, TC, and OTC in milk samples were 103–106.8%, 99.8–106.7%, and 91–105.3%, respectively; while those in pork samples were 96.6–106.4%, 90.2–102.1%, and 89.7–102.1%, respectively. The RSD values were all not higher than 6.5%, indicating good recovery results. In addition, the reliability and accuracy of the ratiometric fluorescent sensor are demonstrated by comparing the HPLC data with the fluorescence measurement results. None of the three antibiotics were detected in samples without the addition of DOX, TC, and OTC, suggesting that there were no residues of these three antibiotics in the samples. These results demonstrate that the proposed method has good application prospects.
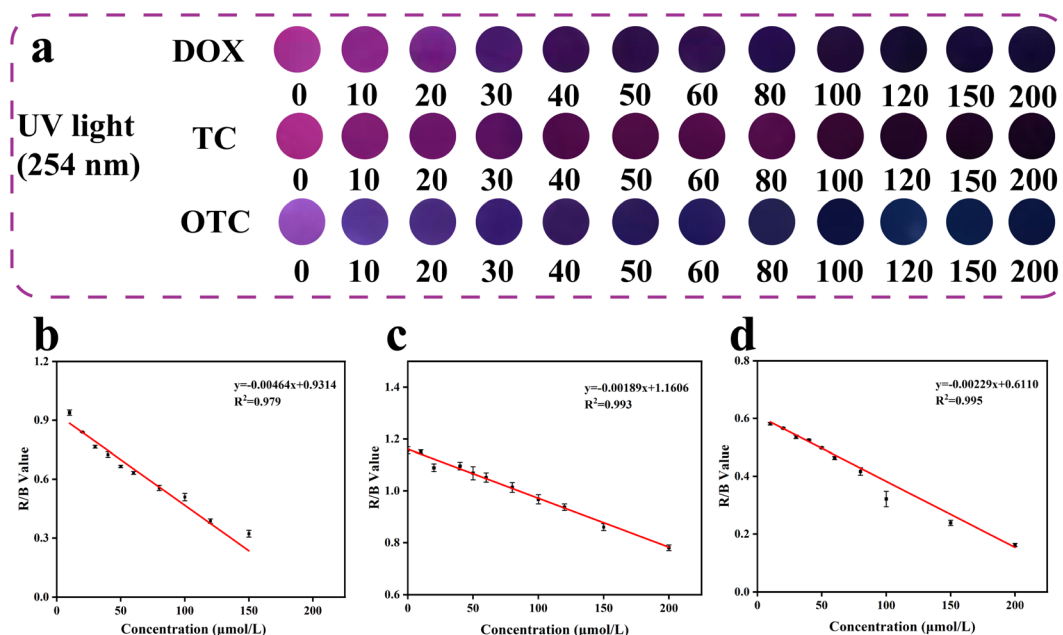

Fig. 7 NH_2-BDC-Eu-DPA hydrogels containing different concentrations (μmol L^{-1}) of DOX, TC, and OTC under 254 nm UV light (a); the R/B value derived from the hydrogel-based sensor plotted against the concentrations of DOX (b), TC (c), and OTC (d).

Table 1 Detection of DOX, TC, and OTC in actual samples

Samples	TCs	Detection of concentration ($\mu mol\ L^{-1}$)	Found concentration ($\mu mol\ L^{-1}$)		Recovery (%)	RSD ($n = 3$, %)	Images by fluorescent hydrogels
			NH$_2$-BDC-Eu-DPA	HPLC			
Milk	DOX	0	ND	ND	—	—	
		10	10.66	7.9	106.6	0.4	
		60	61.79	60.6	103	1.1	
		125	133.54	122.7	106.8	0.2	
	TC	0	ND	ND	—	—	
		10	10.67	8.1	106.7	2.3	
		60	59.85	59.2	99.8	0.9	
		125	129.06	125.7	103.3	0.1	
	OTC	0	ND	ND	—	—	
		10	10.53	8.2	105.3	3.6	
		60	54.58	60.6	91	0.7	
		125	123.29	125.6	98.6	1	
Pork	DOX	0	ND	ND	—	—	
		10	10.09	9.6	100.9	1.5	
		60	57.99	53.0	96.6	1.4	
		125	133	126.3	106.4	1.5	

Table 1 (Contd.)

Samples	TCs	Detection of concentration (μmol L^{-1})	Found concentration (μmol L^{-1}) NH$_2$-BDC-Eu-DPA	HPLC	Recovery (%)	RSD ($n = 3$, %)	Images by fluorescent hydrogels
	TC	0	ND	ND	—	—	
		10	9.02	8.4	90.2	6.5	

Samples	TCs	Detection of concentration (μmol L^{-1})	Found concentration (μmol L^{-1})		Recovery (%)	RSD ($n = 3$, %)	Images by fluorescent hydrogels
		60	61.28	57.6	102.1	1.8	
		125	125.19	124.7	100.2	0.4	
	OTC	0	ND	ND	—	—	
		10	9.58	8.0	95.8	2.8	
		60	53.85	60.9	89.7	0.9	
		125	127.64	125.7	102.1	0.5	

4. Conclusions

In conclusion, a dual-emission fluorescence detection method based on a dual-ligand europium-based MOF (NH$_2$-BDC-Eu-DPA) was successfully established, enabling accurate and rapid detection of TCs (DOX, TC, OTC) in milk and pork. This probe achieves dual emissions at 427 nm and 617 nm under a single excitation wavelength (260 nm). Quantitative analysis is realized through the fluorescence intensity ratio (F_{427}/F_{617}), with a wide linear range (1–200 μmol L^{-1}) and low detection limit, meeting the requirements of actual detection. The purple fluorescence intensity of the hydrogel gradually decreases with increasing TCs concentration, showing a good linear relationship. Selectivity and anti-interference tests showed the probe can specifically recognize TCs, unaffected by other common antibiotics, ions, or biological macromolecules. In actual sample detection, spiked recoveries of milk and pork samples were good, indicating high method accuracy. Also, the method is easy to operate, has a rapid response (reaching steady state quickly), needs no complex instruments, and shows potential for on-site detection. The fluorescent detection approach established in this research offers a novel strategy for the effective surveillance of tetracycline antibiotic residues in animal-derived food products and holds promising application potential in the realm of food safety.

Author contributions

Ruipeng Guo, funding acquisition, project administration, data curation, writing – original draft. Sujiao He, methodology, formal analysis. Bing Zhu, software, validation, resources. Zhiwen Xi, investigation, resources. Jiaxin Wang, software, validation. Mingsha Jie, supervision; project administration; writing – review & editing.

Conflicts of interest

No potential conflicts of interest were identified.

Data availability

The datasets supporting this article have been uploaded as part of the article. Data will be made available on request.

Supplementary information (SI) is available. See DOI: https://doi.org/10.1039/d5ra08234j.

Acknowledgements

References

1 P. Kovalakova, L. Cizmas, T. J. Mcdonald, B. Marsalek, M. Feng and V. K. Sharma, *Chemosphere*, 2020, **251**, 126351.

2 H. Noor, M. Taimoor, T. M. Javed, S. Yasmin, A. Asmar, S. Zaib and S. Hussain, *Bio. Nano. Sci.*, 2025, **15**, 349.

3 L. Xu, H. Zhang, P. Xiong, Q. Zhu, C. Liao and G. Jiang, *Sci. Total Environ.*, 2021, **753**, 141975.

4 X. An, X. Zhu, J. Liu, L. Zou, G. Li and B. Ye, *Spectrochim. Acta, Part A*, 2022, **269**, 120775.

5 C. Xiao, J. Yuan, L. Li, N. Zhong, D. Zhong, Q. Xie, H. Chang, Y. Xu, X. He and M. Li, *Environ. Sci. Ecotechnology*, 2023, **14**, 101–109.

6 C. Wei, Y. Liu, A. Jiang and B. Wu, *Int. J. Clin. Pharmacol.*, 2022, **44**, 709–716.

7 C. Li, Y. Ma, C. Fan, J. Kang and S. Ma, *J. Food Compos. Anal.*, 2024, **133**, 106367.

8 S. Sun, Z. Li, J. Zhu, S. Lv, J. Zhao, X. Yang, Y. Liu, L. Wang and W. Chen, *J. Chromatogr. A*, 2025, **1746**, 465800.

9 C. Bo, W. Zhao, Y. Li, Y. Li, X. Tang and S. Guo, *Microchem. J.*, 2024, **200**, 110403.

10 D. S. Aga, S. O'Connor, S. Ensley, J. O. Payero, D. Snow and D. Tarkalson, *Agric. Food Chem.*, 2005, **53**, 7165–7171.

11 S. Liu, S. Li and S. Gao, *Chem. Eng. J.*, 2024, **484**, 149517.

12 P. Sang, G. Lu, D. Yu, X. Song, Y. Guo, Y. Xie, W. Yao, H. Qian and Z. Hu, *J. Agric. Food Chem.*, 2022, **70**, 39.

13 M. Jie, A. Zhu, J. He, B. Liu, X. Yue, Z. Xu and Y. Bai, *Food Chem.*, 2025, **493**, 145721.

14 W. Zhang, Z. Sun, Y. Tian, Y. Mou, Y. Guo, F. Sun and F. Li, *Sens. Actuators, B*, 2024, **406**, 135427.

15 Y. Liu, H. Guo, N. Wu, L. Peng, M. Wang, J. Tian, J. Xu and W. Yang, *ACS Appl. Nano Mater.*, 2023, **6**, 6627–6636.

16 D. Manoj, S. Rajendran, M. Murphy, A. A. Jalil and C. Sonne, *Chemosphere*, 2023, **340**, 139820.

17 H. Dong, L. Li and C. Li, *Chem. Sci.*, 2023, **32**, 8507.

18 H. Dong, L. Li, Z. Feng, Q. Wang, P. Luan, J. Li and C. Li, *ACS Mater. Lett.*, 2023, **5**, 2656–2664.

19 Y. Wang, X. Tian, H. Zhang, Z. Yang and X. Yin, *ACS Appl. Mater. Interfaces*, 2018, **10**, 22445–22452.

20 Y. Cui, F. Chen and X. Yin, *Biosens. Bioelectron.*, 2019, **135**, 208–215.

21 T. Sun, R. Fan, R. Xiao, T. Xing, M. Qin, Y. Liu, S. Hao, W. Chen and Y. Yang, *J. Mater. Chem. A*, 2020, **8**, 5587–5594.

22 X. Yue, L. Fu, Y. Li, S. Xu, X. Lin and Y. Bai, *Food Chem.*, 2023, **410**, 135390.

23 X. Huo, Y. Xie, Y. Hu, Z. Wang, Y. Sheng, H. Qi, H. Shao, Q. Ma, W. Yu and X. Dong, *J. Colloid Interface Sci.*, 2025, **699**, 138276.

24 B. Li, X. Liao and L. Wang, *Food chem.*, 2025, **489**, 144872.

25 X. Yue, L. Fu, J. Zhou, Y. Li, M. Li, Y. Wang and Y. Bai, *Food Chem.*, 2024, **432**, 137213.

26 Z. Lian, M. Zhao, J. Wang and R. Yu, *J. Sens. Actuators, B.*, 2021, **346**, 130465.

27 Z. Yang, M. Wang, X. Wang and X. Yin, *Anal. Chem.*, 2017, **89**, 1930–1936.

28 L. He, X. Yang, K. Xu and W. Lin, *Anal. Chem.*, 2017, **89**, 9567–9573.

29 C. Zhang, M. Liu, T. Li, S. Liu, Q. Chen, J. Zhang and K. Zhang, *Dyes Pigm.*, 2020, **180**, 108507.

30 A. Das, M. Saikh, A. Misra, M. Ali, P. Pradhan, N. Sepay, S. Dhibar, M. Afzal, S. Abbas and N. Sepay, *J. Mol. Struct.*, 2025, **1352**, 144012.

31 A. Das, A. Misra, M. Ali, M. Saikh, S. Dhibar, K. Banerjee, G. Ghatak, D. Mal, M. Shitf and S. Biswa, *RSC Adv.*, 2025, **15**, 35844–35858.

32 A. Das, M. Ali, A. Misra, S. Islam, B. Kar, S. Biswas, G. Ghatak, D. Mal, M. Shit, M. Dolai and A. Das, *Appl. Organomet. Chem.*, 2024, **39**, 1.

33 Y. Sun, Y. Cheng and X. Yin, *J. Anal. Chem.*, 2021, **93**, 3559–3566.

34 M. Jie, S. Lan, B. Zhu, A. Zhu, X. Yue, Q. Xiang and Y. Bai, *Food Chem.*, 2024, **458**, 140304.

35 R. Yao, Z. Li, G. Liu, C. Fan and S. Pu, *Talanta*, 2021, **234**, 122612.

36 Q. Zhang, X. Feng, C. Fang and L. Guo, *J. China Stand.*, 2023, **15**, 223–227.

37 H. Zheng, X. Jiang, Y. Wang, G. Zhang, B. Zhang and Q. Zhang, *J. Colloid Interface Sci.*, 2025, **716**, 136715.

38 T. Naderipour and G. E. Lemraski, *J. Chem. Select.*, 2024, **9**, 9.

39 Z. Fang, Z. Deng, X. Wan, Z. Li, X. Ma, S. Hussain and X. Peng, *Appl. Catal., B*, 2021, **296**, 120329.

40 J. Yao, M. Xie and Y. Li, *Microporous Mesoporous Mater.*, 2021, **317**, 110831.

41 A. Sharma, A. Sharma, R. Kataria, N. Mehta and S. K. Mehta, *J. Environ. Chem. Eng.*, 2025, **13**, 117381.

42 P. Wu, H. Li, X. Zhao and W. Zhao, *Inorg. Chim. Acta*, 2025, **581**, 122624.

43 C. Fu, X. Feng, H. Tian, Y. Zhang, Z. Zhai, P. Qiu, C. Hu, J. Liu and J. Wang, *Appl. Surf. Sci.*, 2025, **702**, 163380.